FULL RESEARCH ARTICLE

Subtle change in the work hardening behavior of fcc materials processed by selective laser melting

R. Sokkalingam[1] · K. Sivaprasad[1] · N. Singh[2] · V. Muthupandi[1] · P. Ma[3] · Y. D. Jia[4] · K. G. Prashanth[5,6,7]

Abstract

Single face centered cubic (fcc) AISI (American Iron and Steel Institute)-316L stainless steel and CoCrFeMnNi-high entropy alloy (HEA) were successfully fabricated using selective laser melting (SLM). Both the SLM processed alloys reveal the presence of hierarchical microstructure (presence of columnar grains, and cellular substructures). Also, the microhardness and tensile properties of AISI 316L stainless steel and CoCrFeMnNi-HEA are similar, where the microhardness varies between 240 and 270 $HV_{0.5}$ and the yield strength and ultimate tensile strength are observed to be around ~ 500 MPa and ~ 600 MPa respectively. The aim of this research is to study the influence of rapid work hardening vs steady state working hardening in two materials of same crystal structure. Accordingly, CoCrFeMnNi-HEA exhibits higher work hardening rate at lower strains (< 5% true strain); however, it lacks its work hardening stability at higher strain. While in case of AISI 316L stainless steel, even though, it shows lower work hardening at initial strain, it withstands at higher strain (high ductility) due to stable work hardening ability by twin mediated plasticity during plastic deformation.

✉ K. G. Prashanth
kgprashanth@gmail.com

[1] Advanced Materials Processing Laboratory, Department of Metallurgical and Materials Engineering, National Institute of Technology, Tiruchirappalli, Tamil Nadu 620015, India

[2] Department of Mechanical and Industrial Engineering, Tallinn University of Technology, Ehitajate tee 5, 19086 Tallinn, Estonia

[3] School of Materials Engineering, Shanghai University of Engineering Science, Shanghai 201620, China

[4] School of Materials Science and Engineering, Shanghai University, Shanghai 200444, China

[5] Department of Mechanical and Industrial Engineering, Tallinn University of Technology, Ehitajate tee 5, 19086 Tallinn, Estonia

[6] Erich Schmid Institute of Materials Science, Austrian Academy of Sciences, Jahnstraße 12, 8700 Leoben, Austria

[7] CBCMT, School of Mechanical Engineering, Vellore Institute of Technology, Vellore 632014, India

1 Introduction

Metal additive manufacturing (MAM) is a revolutionizing manufacturing process recently substituting the conventional manufacturing processes owing to its capability to develop near-net-shaped components in a single step via layer by layer fashion with minor or no requirement of post-processing, significant part reduction, etc. [1–3]. Selective laser melting (SLM) is one such metal additive manufacturing technique, which overpasses other techniques due to its ability to produce intricate structures of any shape (theoretically) as unused powders act as the virtual tooling/ die/ mold for the complex design [1, 4]. SLM has the capability to manufacture a wide range of metallic materials like Al-based alloys (Al-Si, AlSi10Mg and high strength Al-based alloys like 2XXX and 7XXX) [5–8], Fe-based materials (316L stainless steel, 17-4PH stainless steel, tool steels) [9–11], Ni-based superalloys (IN718 alloy) [12–14] and Ti-based alloys (Ti6Al4V, TNZT) [15–18]. Recently, the material spectrum has been extended towards processing of novel materials like face centered cubic (fcc) high entropy alloys (HEA) like CoCrFeNi [19], CoCrFeMnNi [20], Al_xCoCrFeNi [21], AlCrFeNiV [22], metallic glasses [23–25], etc.

HEAs are also known as multi principal element alloys that found their importance after their discovery in 2004 [26, 27]. The fcc phased HEAs (like CoCrFeMnNi-HEA and $Al_{0.1}CoCrFeNi$-HEA) show superior damage-tolerance properties, especially at a cryogenic temperature [28, 29]. This is due to its synergy with plasticity and shielding mechanism and high lattice friction, exceptional irradiation resistance [30, 31], and low high temperature softening (negligible creep) [32] compared to the commercially available alloys like austenitic stainless steel (304L, 316L, M316 stainless steel), and pure Zr and Ni-based superalloys. However, relatively lower yield strength due to a fcc crystal structure makes the material inferior. Several efforts were taken to enhance the yield strength of these alloys by thermo-mechanical processing (forging [29, 33], rolling [34] followed by heat treatment), friction stir processing [35], dispersion of nanoparticles [36], etc. SLM can improve the strength of the fabricated materials by producing hierarchical microstructures with finer cellular substructures with a higher density of dislocations due to the rapid heating and cooling rate involved in the process [37–40].

Zhu et al. found that SLM of CoCrFeMnNi-HEA could result in the formation of the hierarchical microstructure ranging from millimeters to nanometer scale (like melt pool, columnar grains, cellular substructure, and dislocations) [20]. In addition, higher strength in SLMed CoCrFeMnNi-HEA than the cast alloy was observed, which may be attributed to the dislocation hardening in these cellular structures [20]. On the other hand, Li et al. have found the presence of nano-twins and nano-scale tetragonal σ phase in the as-SLMed CoCrFeMnNi-HEA sample, due to rapid solidification [40]. Further, the strength of the SLM processed CoCrFeMnNi-HEA was improved by post-processing (hot isostatic pressing) as the consequence of reduced porosity and defects [41]. Further, recent research has depicted the possibility of tailoring the microstructure (columnar or cellular) and texture by changing the scanning strategy [42]. Kim et al. found the presence of nano-oxide particles in SLMed CoCrFeMnNi-HEA along with the inclusions of nano-Mn_2O_3. Also found are room and high temperature strengthening factors for the alloy [43, 44].

Even though a handful of works were carried out on the single fcc phased CoCrFeMnNi-HEA, most of them were concentrated on the microstructural studies and subsequent evaluation of their strengthening mechanisms. In addition, some of the reports compared the superiority of CoCrFeMnNi-HEA with their as-cast counterparts. Recently, fcc

phased HEAs are being substituted in the place of austenitic stainless steel in the nuclear power plant, aerospace, and automobile applications by employing dissimilar welding between $Al_{0.1}CoCrFeNi$-HEA and austenitic stainless steels [45]. Further, CoCrFeMnNi-HEA coating on the carbon steel was employed to enhance the corrosion resistance and to study the feasibility of using CoCrFeMnNi-HEA over the commercially used corrosion-resistant 316L stainless steel [46]. The aim of this research is to study the influence of rapid work hardening vs steady state working hardening in two materials of same crystal structure. Accordingly, the present work analyzes the microstructure evolution, phase, and related mechanical properties of CoCrFeMnNi-HEA processed by SLM and compare the same with the conventional 316L stainless steel (also produced by SLM).

2 Materials and methods

2.1 Additive manufacturing of HEA and stainless steel

Single fcc-based alloys: AISI (American Iron and Steel Institute)-316L stainless steel and CoCrFeMnNi-HEA were prepared by gas-atomization were used as the feedstock material for the present study. The average particle size of the AISI 316L stainless steel and CoCrFeMnNi-HEA powders are 31 ± 10 μm and 33 ± 11 μm respectively with particle size distribution ranging from 10 to 100 μm. Further the chemical composition of the powders by energy dispersion spectroscopy (EDS) analysis is given in the Table 1. Selective laser melting device (ReaLizer GmbH make, Model: SLM50) equipped with Yb-YAG laser source with a maximum laser power of 120 W and a spot size of ~30 μm was used for the fabrication process. The processing parameters for AISI 316L stainless steel and CoCrFeMnNi-HEA are given in the Table 1. Processing parameter for AISI 316L stainless steel is already available for the machine. To optimize the process parameters for the CoCrFeMnNi-HEA, cubes of size $10 \times 10 \times 10$ mm^3 were fabricated by keeping the focal length, layer thickness, hatch distance, hatch offset, point distance and hatch rotation constant and varying the exposure time (25, 30, 40, 60, and 80 μs) and laser power (60, 72, 84, and 96 W). The fabrication of these samples was performed in an Ar environment (such that the oxygen content in the chamber was maintained below 0.1 ppm to avoid any possible oxidation during the fabrication process). Apart

Table 1 Chemical composition of AISI 316L stainless steel and CoCrFeMnNi-HEA (wt%)

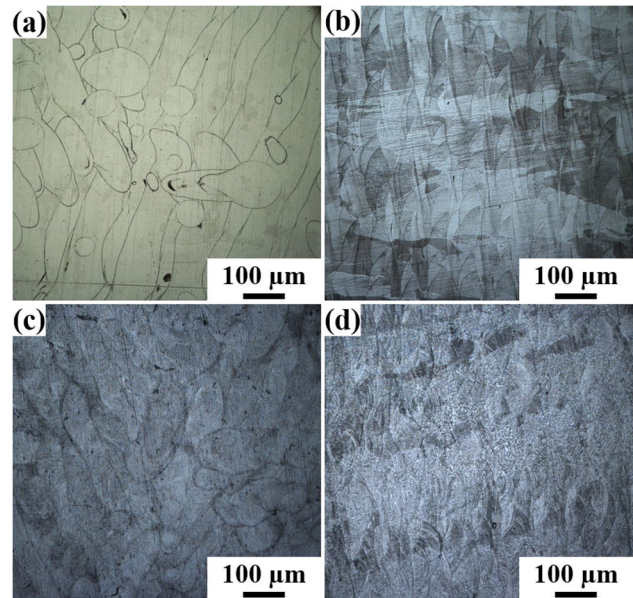| Elements	Co	Cr	Fe	Mn	Ni	Mo	Si
AISI 316L	–	17.9 ± 0.7	64.6 ± 0.1	1.9 ± 0.1	12.2 ± 0.7	2.6 ± 0.2	1.0 ± 0.1
CoCrFeMnNi	19.5 ± 0.2	19.75 ± 0.25	19.76 ± 0.35	21.97 ± 0.82	19.00 ± 0.32	–	–

from the cubic samples, the tensile samples (according to the dimensions given in [47]) were printed from CoCrFeMnNi-HEA powder by using the optimized parameter (exposure time – 25 μs and laser power – 96 W respectively) and from 316L stainless steel powder by using the following optimized parameters: exposure time – 25 μs and laser power – 60 W, respectively (Table 2).

2.2 Characterization and mechanical testing

The longitudinal and cross-section of the bulk SLMed AISI 316L stainless steel and CoCrFeMnNi-HEA were polished following the standard metallographic procedure. X-ray diffraction was carried out by scanning the samples with Cu-Kα radiation in the 2θ range 30° and 90° with a step size of 0.05° in Rigaku, Germany (UltimaIII). The polished samples were then etched with Aquaregia (HNO_3 and HCl in 3:1 ratio) for HEAs and Kalling's No. 2 reagent (5 g of $CuCl_2$, 100 ml of HCl, and 100 ml of C_2H_5OH) for AISI 304 stainless steel. The microstructures were observed using an optical microscope (OM) and HITACHI S-3000H scanning electron microscope (SEM). The Vickers microhardness measurements were carried out along the longitudinal using the MICRO MET 2001 device with a load of 500 g and a dwell time of 10 s. The tensile samples were tested under tensile load at a strain rate of 10^{-2}/s using an Instron device.

3 Results and discussion

The microstructure of the SLMed AISI 316L stainless steel and CoCrFeMnNi-HEA observed along the cross-section and longitudinal side of the sample under OM are given in Fig. 1a–d respectively. The microstructure (cross-section) shows the presence of numerous overlapped laser weld tracks and intersection of these tracks at the intersecting points of the islands. Microstructure along the longitudinal (building) direction reveals the layer-by-layer macrostructure

Table 2 SLM processing parameters for AISI 316L stainless steel and CoCrFeMnNi-HEA

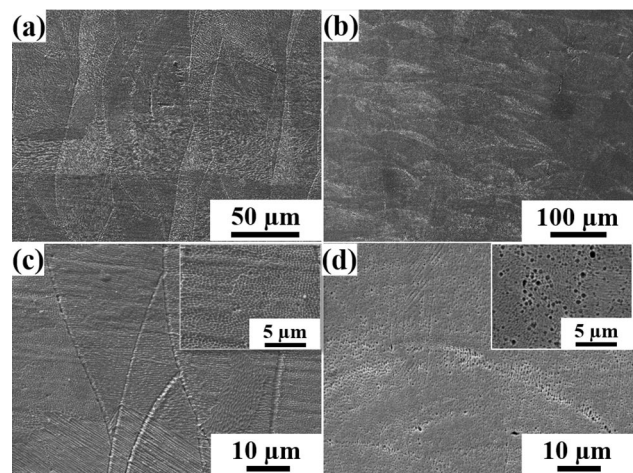| Parameters	AISI 316L stainless steel	CoCrFeMnNi-HEA
Focal length [μm]	25	
Layer thickness [μm]	25	
Hatch distance [μm]	60	
Hatch offset [μm]	50	
Point distance [μm]	20	
Exposure time [μs]	25	25, 30, 40, 60 and 80
Laser power [W]	60	60, 72, 84 and 96
Hatch rotation/layer	60°	

Fig. 1 Optical microscopy images of AISI 316L stainless steel along the **a** cross section and **b** longitudinal directions and CoCrFeMnNi-HEA along the **c** cross-section and **d** longitudinal directions

with numerous semi-elliptical scan tracks like structure as visible in the weld pool in the welding as represented in Fig. 1b, d (OM image) and Fig. 2a, b (SEM image). Further, it can be observed that the columnar grain growth extends over several layers by epitaxial grain growth phenomenon, due to melting and re-melting of the pre-solidified layer of alloys. As, additive manufacturing is the multi-pass welding of the feedstock (powders) layer-by-layer, it starts with building of support structures on substrate and ends with the final designed complex component. Thus, the microstructure


Fig. 2 Scanning electron microscopy images of the SLMed **a** AISI 316L stainless steel and **b** CoCrFeMnNi-HEA in the longitudinal direction at lower magnification and its higher magnification images (**c**) and (**d**) and insets showing the cellular morphology

evolution during solidification in the additively manufactured samples also follows structure evolution during similar welding; where epitaxial growth is observed when the melt pool chemical composition remains same [27] or matches with the unmelted base metal [48]. The SLMed AISI 316L stainless steel and CoCrFeMnNi-HEA has expressed the epitaxial growth of the columnar grains from the partially melted grains of earlier built layer over several layers as in Fig. 1b and d (OM image) and Fig. 2a and b (SEM image). This is attributed to the matching composition of each layer of the build material and favourable orientation of the grains along the maximum thermal gradient direction over many layers of the build.

Furthermore, observation of each grain in SLMed AISI 316L stainless steel and CoCrFeMnNi-HEA at higher magnification [Fig. 2 (c,d and insets)] shows the presence of the very fine dendritic cellular features with columnar substructures. Such finer microstructure evolution in the SLMed alloys is due to the high cooling rates ($\sim 10^4$–10^6 K/s) observed during the process [23, 49]. The average size of the cellular structure in AISI 316L stainless steel is ~ 0.5 μm and that of CoCrFeMnNi-HEA is ~ 0.35 μm. Finer cellular features observed in the HEA samples (compared to 316L stainless steel) could be attributed to the in-process characteristics i.e., high applied laser power for HEA. In addition, material characteristics like high temperature structural stability and sluggish cooperative diffusion in HEA also contribute to the finer cellular size. The microstructure of both SLMed AISI 316L stainless steel and CoCrFeMnNi-HEA show hierarchical microstructures, starting from macroscopic scale, weld pools/scan tracks, columnar grains, and cellular dendritic structures. Such occurrence of hierarchical microstructure for 316L stainless steel and CoCrFeMnNi-HEA is in line with other research reports [20, 50–52].

X-ray diffraction (XRD) patterns of the feedstock powders and the SLMed AISI 316L stainless steel and CoCrFeMnNi-HEA in longitudinal and cross-section are given in Fig. 3. XRD patterns of the gas-atomized AISI 316L and CoCrFeMnNi-HEA powders show dominant diffraction peaks corresponding to fcc structure with a minor secondary peak near the diffraction angle 45°. This minor peak (110) belongs to bcc phase. Recent studies on gas atomized 316L powder depicts that this minor bcc peak indicates the presence of high-temperature δ-ferrite [53, 54]. Yang et al. have reported the presence of a minor bcc phase in CrFeNiMn-HEA and is indirectly related with the size of the atomized powder particle (both in the cases of high-speed steel [55] and CrFeNiMn-HEA powders [56] respectively). Smaller particles with least nucleant could experience higher degree of supercooling than that of the larger particle [56]. Kelly et al. proposed that the bcc phase evolution could be higher in smaller particles in 303 stainless steels, where degree of supercooling is very high as the consequence of isolation
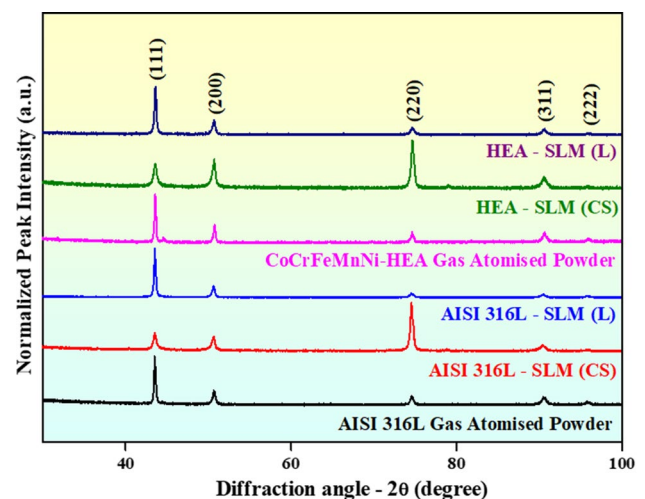
Fig. 3 X-ray diffraction patterns of the feed stock powders and SLMed AISI 316L stainless steel, and CoCrFeMnNi-HEA in cross section (CS) and longitudinal (L) directions respectively

of heterogeneous nucleation catalyst [57]. In addition, it was found that there would be solute partitioning (a) with respect to Cr and nickel (fcc structure) and (b) Cr, Ni and Mn (bcc structure) during rapid cooling. It can be supported with other findings that, the bcc phase will tend to form in CrFeNiMn-based alloys, when the Cr content is higher than 18 wt% [58]. Hence, such phase transformation in atomized powders is attributed to the cooling rate and the chemical composition effect.

XRD patterns along the longitudinal and cross-section directions are completely different, where the highest intense peak for the longitudinal direction is along the (111) plane. However, in case of the cross section direction, the highest intense peak is orientated towards (220) plane, showing the presence of texture. The minor bcc phase, which was observed in the feedstock powders is absent in both bulk SLMed AISI 316L stainless steel and CoCrFeMnNi-HEA samples. A similar trend in longitudinal direction was reported by Li et al. [41]. The relatively large volume of melt pool (compared to the size of the small powder particles) allows the possibility of several nucleation sites and subsequently stabilizes the crystal growth resulting in the formation of crystals with a single fcc phase. Also, heterogeneous nucleation sites existing on the partially melted grains at the melt pool/solid surface interface of the fcc crystal guides the solidifying material to grow epitaxially along easy growth direction < 100 > along the building direction. In addition, the SLM processing of the gas-atomized powder has resulted in relative broad XRD peaks for both 316L stainless steel and HEA [17, 40, 43]. Such broadening could be attributed to either the existence of the residual stress due to laser processing or coexistence of two fcc phases with different lattice parameters as found in the EBM processing of 316L

stainless steel [52]. In addition, excess volume of defects like the dislocation density may also lead to the broadening of the peaks along with the size effect.

Further, it is obvious from the XRD patterns, the highest intense peaks for the SLM samples examined in the longitudinal, and cross-section are different. It indicates the presence of preferential growth (texture) in the bulk-processed sample observed along the different planes. For evaluating this, the XRD pattern of the gas atomized powder is taken as the reference and the texture coefficients along the longitudinal and cross-section were evaluated by using the equation in [59] and tabulated (Table 3). The texture of the grains in the longitudinal is significantly oriented towards < 111 > and < 200 > planes respectively, while that of cross section is towards < 220 >. Even though the easy grain growth direction is < 100 > for the cubic crystals, the texture can be varied with applied energy density, sample

Table 3 Texture co-efficient in different planes in the SLMed AISI 316L stainless steel and CoCrFeMnNi-HEA

| Texture coefficient (T_c)	AISI 316L stainless steel		CoCrFeMnNi-HEA	
	Cross-section	Longitudinal	Cross-section	Longitudinal
T_c (111)	0.2824	1.6565	0.3182	1.1590
T_c (200)	0.6936	1.2476	0.9500	1.0923
T_c (220)	2.9850	0.6963	2.2441	0.9980
T_c (311)	0.5945	0.6776	0.8237	0.9543
T_c (222)	0.4572	0.7188	0.6509	0.7968

thickness as well as with change in the scanning strategies. Piglione et al. has reported the preferential grain growth along the < 200 > direction in the SLM processed CoCrFeMnNi-HEA, while using bidirectional scanning strategy without any scan rotation over the layers [42]. While Li et al. have reported formation of isotropous grain feature (grain orientation in < 100 >, < 110 > and < 111 > directions) and < 100 > and < 110 > preferential grain orientation along the cross section, when CoCrFeMnNi-HEA is additively manufactured (SLMed) using long scan vectors and with the employment of 67° scan rotation between layers [41]. The isotropous grain feature is attributed to the instantaneous change in the favourable grain growth direction over the length of the melt pool with varying thermal gradient direction and the scanning direction, when measured along the longitudinal direction [60]. Zhu et al. on other hand found preferential growth along the < 001 > and < 101 > directions with few grains oriented towards < 111 > direction, when a scan rotation of 90° between layers was used [20]. Hence, the mixed texture in the current study could be attributable to the scanning strategy used i.e., bidirectional scanning with the hatch rotation of 60° between layers.

The representative microhardness distribution and average microhardness in SLMed AISI316L stainless steel and CoCrFeMnNi-HEA is given in Fig. 4a, b and Table 3 respectively. The microhardness distribution for the SLMed AISI316L stainless steel is concentrated mostly within the range of 240 to 260 $HV_{0.5}$. In case of CoCrFeMnNi-HEA, it shows even distribution of the microhardness, with the hardness values ranging between 250 and 270 $HV_{0.5}$. Overall, both the AISI

Fig. 4 Vickers microhardness ($HV_{0.5}$) distribution matrix for SLM processed **a** AISI 316L stainless steel and **b** CoCrFeMnNi-HEA. **c** Engineering stress–strain plot and (d) Kocks-Mecking work hardening plot of SLM processed AISI 316L stainless steel and CoCrFeMnNi-HEA respectively
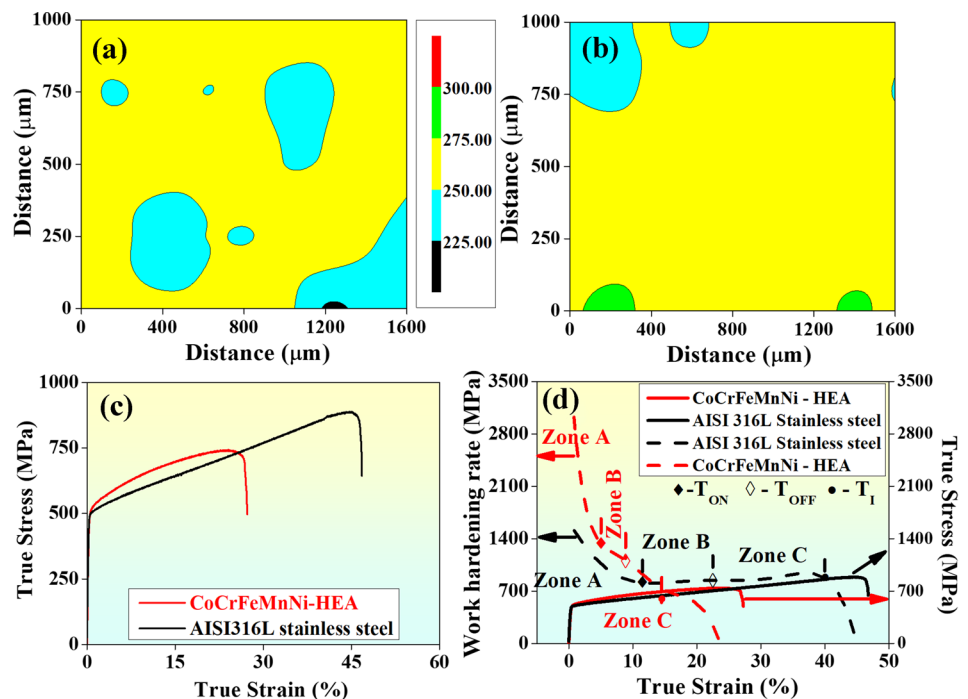
316L stainless steel and CoCrFeMnNi-HEA show similar hardness variation within experimental errors with the average hardness observed to be 255 ± 10 $HV_{0.5}$ and 259 ± 4 $HV_{0.5}$ for AISI 316L stainless steel and CoCrFeMnNi-HEA, respectively. The engineering stress–strain plots of the SLMed AISI 316L stainless steel and CoCrFeMnNi-HEA are given in Fig. 4c. Further, the yield strength (YS), ultimate tensile strength (UTS) and % elongation were evaluated and tabulated in Table 4. The YS and UTS of the AISI 316L stainless steel is 500 ± 5 MPa and 570 ± 10 MPa respectively with 58% ductility. In case of CoCrFeMnNi-HEA, the YS and UTS is observed to be 516 ± 6 MPa and 600 ± 12 MPa, respectively with a ductility of $\sim 31\%$, which is in agreement with other reports on CoCrFeMnNi-HEA [28, 52]. Like microhardness, tensile strength of AISI 316L stainless steel and CoCrFeMnNi-HEA are similar, however, CoCrFeMnNi-HEA shows higher work hardening behaviour with relatively moderate ductility. In order to compare the statistically work hardening rate (WHR)—$(d\sigma/d\varepsilon)$ was evaluated for SLMed AISI 316L stainless steel and CoCrFeMnNi-HEA by Kocks-Mecking method [61–63]. Figure 4d shows the Kocks-Mecking plot (WHR vs true strain) and true stress–strain plot for SLMed AISI 316L stainless steel and CoCrFeMnNi-HEA respectively.

WHR vs true strain plot of AISI 316L stainless steel show three different zones (indicated as Zone A, Zone B and Zone C) with different rates of work hardening. Zone A (less than 12% true strain) reveals a sharp decrease in the WHR due to slip deformation of material (dislocation slip-dominated plasticity). With an increase in true stress beyond 12% (the twinning onset point T_{on}), the WHR increases steadily up to a transition point called twinning offset point, T_{off} (true strain of 21%) in Zone B (twinning mediated plasticity). Such an increase in the WHR is attributed to the restriction of dislocation motion and mean free path reduction by the deformation induced twins. After, T_{off}, when the stress and strain increases, the dislocations overpass the twins and grain boundaries by cross gliding and the dislocation moves again by dislocation slip gliding in Zone C and reaches plastic instability at point T_I ($d\sigma/d\varepsilon = \sigma$) with increase in strain and fails eventually [62]. This multi-stage strain hardening is typical in twin-induced plasticity (TWIP) steels [27]. WHR vs true strain plot of CoCrFeMnNi-HEA also reveals three distinct zones; however, the trend is completely different from that of AISI 316L stainless steel. In Zone A ($< 5\%$ true strain), WHR drops sharply compared to that of AISI

316L stainless steel, which may be attributed to excessive deformation by slip due to more texture coefficient in $< 220 >$ direction compared to AISI 316L stainless steel [36]. In Zone B (between 5 and 9% true strain), the work hardening rate is decreasing, due to onset of the deformation twin, the rate of decrease in the WHR drops until T_{off} and further increase in true strain leads to dislocation slip dominated deformation and finally the sample fails due to plastic instability. Thapliyal et al. shows that the sustained WHR is required for the metallic material to show higher strength and ductility [64]. In the present study, even though AISI 316L stainless steel exhibited less WHR at initial strain values than that of HEA, it shows sustained WHR rate over long range of true strain (12 to 38%). In case of the CoCrFeMnNi-HEA, even though it is initially showing higher WHR due to intrinsic higher friction stress (solid solution strengthening), with increase in true strain the work hardening rate keeps on decreasing and fails earlier than that of AISI 316 stainless steel and shows lower ductility.

The fracture surface of the tensile tested SLMed AISI 316L stainless steel and CoCrFeMnNi-HEA samples is given in Fig. 5. The fracture surface of the AISI 316L stainless steel show smooth features with elliptical periphery and reduced cross section. On the other hand, CoCrFeMnNi-HEA reveals irregular features (with up and downs) in the fracture surface and fails with less plastic deformation, showing a circular periphery [Fig. 5a, b]. Magnified images of Fig. 5a, b are shown in Fig. 5c–f. Relatively clean fracture surfaces are observed for SLMed AISI 316L stainless steel sample, while in case of CoCrFeMnNi-HEA, it reveals the presence of pores, which leads to faster propagation of the cracks, reducing the ductility of the HEA sample. Higher magnification images reveal the presence of fibrous dimples indicating ductile mode of in these samples [Fig. 5c–e]. The size of the dimples observed in the AISI 316L samples is smaller than that of the HEA sample, but uneven surface is observed for the HEA sample compared to the AISI 316L sample. The results suggests that both *fcc* materials (AISI 316L and CoCrFeMnNi-HEA) show similar structure, microstructures and microhardness. The mechanical tests also show similar properties but differences in the ductility and WHRs are observed, which makes the differences in their deformation mechanism.

Table 4 Mechanical properties of the additive manufactured bulk AISI 316L stainless steel and CoCrFeMnNi-HEA samples

Sample designation	Microhardness [$HV_{0.5}$]	Yield Strength [MPa]	Ultimate tensile strength [MPa]	% Elongation
AISI 316L	255 ± 10	500 ± 5	570 ± 10	$\sim 58\%$
CoCrFeMnNi	259 ± 4	516 ± 6	600 ± 12	$\sim 31\%$
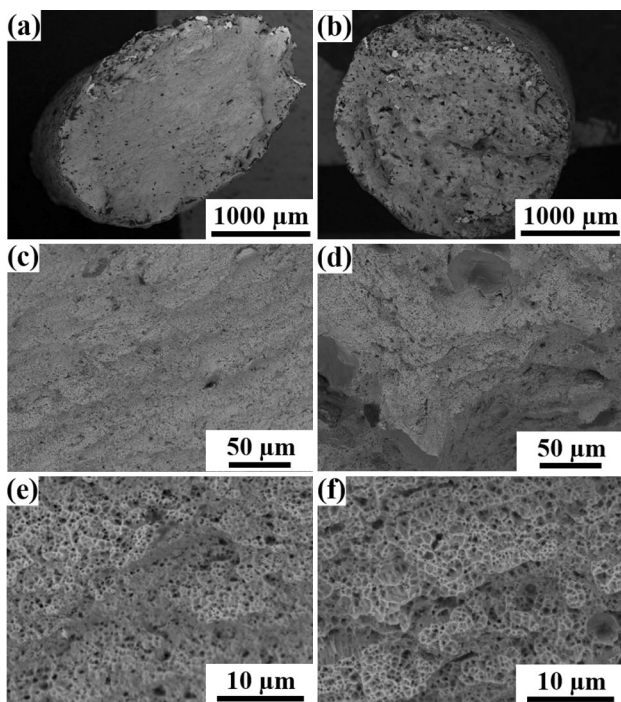
Fig. 5 Scanning electron microscope images of the fracture surfaces of AISI 316L **a**, **c**, **e** and CoCrFeMnNi-HEA **b**, **d**, **f** respectively

4 Conclusion

Single fcc-phased AISI 316L stainless steel and CoCrFeMnNi-HEA were successfully processed using selective laser melting. Both the alloys reveal hierarchical microstructure, columnar grains, and cellular substructures after SLM. The microhardness and tensile properties of AISI 316L stainless steel and CoCrFeMnNi-HEA are similar, where microhardness varies within the range 240–270 $HV_{0.5}$, YS ~ 500 MPa and UTS ~ 600 MPa respectively. Even though CoCrFeMnNi-HEA shows a higher work hardening rate than AISI 316L stainless steel at a lower strain, at higher strain, the work hardening rate of CoCrFeMnNi-HEA decreases tremendously due to weaker twin mediated plasticity. However, AISI 316L stainless steel maintains sustainable WRH, while plastically deforming with twin mediated plasticity at higher strain maintaining higher ductility than that of CoCrFeMnNi-HEA.

Declarations

Conflict of interest The authors have no conflicts of interest to disclose the data.

References

1. DebRoy T, Wei HL, Zuback JS et al (2018) Additive manufacturing of metallic components—process, structure and properties. Prog Mater Sci 92:112–224. https://doi.org/10.1016/j.pmatsci.2017.10.001
2. Herzog D, Seyda V, Wycisk E, Emmelmann C (2016) Additive manufacturing of metals. Acta Mater 117:371–392. https://doi.org/10.1016/j.actamat.2016.07.019
3. Prashanth K, Löber L, Klauss H-J et al (2016) Characterization of 316L steel cellular dodecahedron structures produced by selective laser melting. Technologies 4:34. https://doi.org/10.3390/technologies4040034
4. Ma P, Jia Y, Gokuldoss P, konda, et al (2017) Effect of Al2O3 nanoparticles as reinforcement on the tensile behavior of Al-12Si composites. Metals (Basel) 7:1–11. https://doi.org/10.3390/met7090359
5. Prashanth KG, Scudino S, Klauss HJ et al (2014) Microstructure and mechanical properties of Al-12Si produced by selective laser melting: effect of heat treatment. Mater Sci Eng A 590:153–160. https://doi.org/10.1016/j.msea.2013.10.023
6. Ma P, Prashanth K, Scudino S et al (2014) Influence of annealing on mechanical properties of Al-20Si processed by selective laser melting. Metals (Basel) 4:28–36. https://doi.org/10.3390/met4010028
7. Wang Z, Ummethala R, Singh N et al (2020) Selective laser melting of aluminum and its alloys. Materials (Basel) 13:1–67. https://doi.org/10.3390/ma13204564
8. Prashanth KG, Scudino S, Chaubey AK et al (2016) Processing of Al-12Si-TNM composites by selective laser melting and evaluation of compressive and wear properties. J Mater Res 31:55–65. https://doi.org/10.1557/jmr.2015.326
9. Salman OO, Brenne F, Niendorf T et al (2019) Impact of the scanning strategy on the mechanical behavior of 316L steel synthesized by selective laser melting. J Manuf Process 45:255–261. https://doi.org/10.1016/j.jmapro.2019.07.010
10. Haghdadi N, Laleh M, Moyle M, Primig S (2020) Additive manufacturing of steels: a review of achievements and challenges. J Mater Sci 561(56):64–107. https://doi.org/10.1007/S10853-020-05109-0
11. Gorsse S, Hutchinson C, Gouné M, Banerjee R (2017) Additive manufacturing of metals: a brief review of the characteristic microstructures and properties of steels, Ti-6Al-4V and high-entropy alloys. Sci Technol Adv Mater 18:584–610. https://doi.org/10.1080/14686996.2017.1361305
12. Marchese G, Garmendia Colera X, Calignano F et al (2017) Characterization and comparison of inconel 625 processed by selective laser melting and laser metal deposition. Adv Eng Mater 19:1600635. https://doi.org/10.1002/adem.201600635
13. Witkin DB, Patel DN, Helvajian H et al (2019) Surface treatment of powder-bed fusion additive manufactured metals for improved fatigue life. J Mater Eng Perform 28:681–692. https://doi.org/10.1007/s11665-018-3732-9
14. Konečná R, Nicoletto G, Kunz L, Bača A (2016) Microstructure and directional fatigue behavior of Inconel 718 produced by selective laser melting. Procedia Struct Integr 2:2381–2388. https://doi.org/10.1016/j.prostr.2016.06.298
15. Gokuldoss PK, Kolla S, Eckert J (2017) Additive manufacturing processes: selective laser melting, electron beam melting and binder jetting-selection guidelines. Materials (Basel) 10:1–11. https://doi.org/10.3390/ma10060672
16. Ummethala R, Jayaraj J, Karamched PS et al (2021) In vitro corrosion behavior of selective laser melted Ti-35Nb-7Zr-5Ta. J Mater Eng Perform. https://doi.org/10.1007/s11665-021-05940-9

17. Ummethala R, Karamched PS, Rathinavelu S et al (2020) Selective laser melting of high-strength, low-modulus Ti–35Nb–7Zr–5Ta alloy. Materialia 14:100941. https://doi.org/10.1016/j.mtla.2020.100941

18. Attar H, Löber L, Funk A et al (2015) Mechanical behavior of porous commercially pure Ti and Ti-TiB composite materials manufactured by selective laser melting. Mater Sci Eng A 625:350–356. https://doi.org/10.1016/j.msea.2014.12.036

19. Brif Y, Thomas M, Todd I (2015) The use of high-entropy alloys in additive manufacturing. Scr Mater 99:93–96. https://doi.org/10.1016/j.scriptamat.2014.11.037

20. Zhu ZG, Nguyen QB, Ng FL et al (2018) Hierarchical microstructure and strengthening mechanisms of a CoCrFeNiMn high entropy alloy additively manufactured by selective laser melting. Scr Mater 154:20–24. https://doi.org/10.1016/j.scriptamat.2018.05.015

21. Shukla S, Choudhuri D, Wang T et al (2018) Hierarchical features infused heterogeneous grain structure for extraordinary strength-ductility synergy. Mater Res Lett 6:676–682. https://doi.org/10.1080/21663831.2018.1538023

22. Yao H, Tan Z, He D et al (2020) High strength and ductility AlCrFeNiV high entropy alloy with hierarchically heterogeneous microstructure prepared by selective laser melting. J Alloys Compd 813:152196. https://doi.org/10.1016/j.jallcom.2019.152196

23. Jung HY, Choi SJ, Prashanth KG et al (2015) Fabrication of Fe-based bulk metallic glass by selective laser melting: a parameter study. Mater Des 86:703–708. https://doi.org/10.1016/j.matdes.2015.07.145

24. Pauly S, Löber L, Petters R et al (2013) Processing metallic glasses by selective laser melting. Mater Today 16:37–41. https://doi.org/10.1016/j.mattod.2013.01.018

25. Li N, Zhang J, Xing W et al (2018) 3D printing of Fe-based bulk metallic glass composites with combined high strength and fracture toughness. Mater Des 143:285–296. https://doi.org/10.1016/j.matdes.2018.01.061

26. Cantor B, Chang ITH, Knight P, Vincent AJB (2004) Microstructural development in equiatomic multicomponent alloys. Mater Sci Eng A 375–377:213–218. https://doi.org/10.1016/j.msea.2003.10.257

27. Yeh J-W, Chen S-K, Lin S-J et al (2004) Nanostructured high-entropy alloys with multiple principal elements: novel alloy design concepts and outcomes. Adv Eng Mater 6:299–303. https://doi.org/10.1002/adem.200300567

28. Zhang ZJ, Mao MM, Wang J et al (2015) Nanoscale origins of the damage tolerance of the high-entropy alloy CrMnFeCoNi. Nat Commun 6:1–6. https://doi.org/10.1038/ncomms10143

29. Li D, Zhang Y (2016) The ultrahigh charpy impact toughness of forged AlxCoCrFeNi high entropy alloys at room and cryogenic temperatures. Intermetallics 70:24–28. https://doi.org/10.1016/j.intermet.2015.11.002

30. Xia SQ, Yang X, Yang TF et al (2015) Irradiation resistance in AlxCoCrFeNi high entropy alloys. JOM 67:2340–2344. https://doi.org/10.1007/s11837-015-1568-4

31. Xu Q, Guan HQ, Zhong ZH et al (2021) Irradiation resistance mechanism of the CoCrFeMnNi equiatomic high-entropy alloy. Sci Rep 11:1–8. https://doi.org/10.1038/s41598-020-79775-0

32. Wang WR, Wang WL, Yeh JW (2014) Phases, microstructure and mechanical properties of AlxCoCrFeNi high-entropy alloys at elevated temperatures. J Alloys Compd 589:143–152. https://doi.org/10.1016/j.jallcom.2013.11.084

33. Sokkalingam R, Sivaprasad K, Duraiselvam M et al (2020) Novel welding of Al0.5CoCrFeNi high-entropy alloy: corrosion behavior. J Alloys Compd 817:153163. https://doi.org/10.1016/j.jallcom.2019.153163

34. Won JW, Lee S, Park SH et al (2018) Ultrafine-grained CoCrFeMnNi high-entropy alloy produced by cryogenic multi-pass caliber rolling. J Alloys Compd 742:290–295. https://doi.org/10.1016/j.jallcom.2018.01.313

35. Kumar N, Komarasamy M, Nelaturu P et al (2015) Friction stir processing of a high entropy alloy Al0.1CoCrFeNi. JOM 67:1007–1013. https://doi.org/10.1007/s11837-015-1385-9

36. Guo L, Gu J, Gan B et al (2021) Effects of elemental segregation and scanning strategy on the mechanical properties and hot cracking of a selective laser melted FeCoCrNiMn-(N, Si) high entropy alloy. J Alloys Compd 865:158892. https://doi.org/10.1016/j.jallcom.2021.158892

37. Wang L, Zhang Q, Zhu J et al (2019) Nature of extra capacity in MoS2 electrodes: molybdenum atoms accommodate with lithium. Energy Storage Mater 16:37–45. https://doi.org/10.1016/j.ensm.2018.04.025

38. Lin YC, Lu N, Perea-Lopez N et al (2014) Direct synthesis of van der Waals solids. ACS Nano 8:3715–3723. https://doi.org/10.1021/nn5003858

39. Wang Z, Xie M, Li Y et al (2020) Premature failure of an additively manufactured material. NPG Asia Mater 12:1–10. https://doi.org/10.1038/s41427-020-0212-0

40. Zhao C, Wang Z, Li D et al (2021) Selective laser melting of Cu–Ni–Sn: a comprehensive study on the microstructure, mechanical properties, and deformation behavior. Int J Plast 138:102926. https://doi.org/10.1016/j.ijplas.2021.102926

41. Li R, Niu P, Yuan T et al (2018) Selective laser melting of an equiatomic CoCrFeMnNi high-entropy alloy: processability, non-equilibrium microstructure and mechanical property. J Alloys Compd 746:125–134. https://doi.org/10.1016/j.jallcom.2018.02.298

42. Piglione A, Dovgyy B, Liu C et al (2018) Printability and microstructure of the CoCrFeMnNi high-entropy alloy fabricated by laser powder bed fusion. Mater Lett 224:22–25. https://doi.org/10.1016/j.matlet.2018.04.052

43. Kim YK, Choe J, Lee KA (2019) Selective laser melted equiatomic CoCrFeMnNi high-entropy alloy: microstructure, anisotropic mechanical response, and multiple strengthening mechanism. J Alloys Compd 805:680–691. https://doi.org/10.1016/j.jallcom.2019.07.106

44. Kim YK, Yang S, Lee KA (2020) Superior temperature-dependent mechanical properties and deformation behavior of equiatomic CoCrFeMnNi high-entropy alloy additively manufactured by selective laser melting. Sci Rep 10:1–13. https://doi.org/10.1038/s41598-020-65073-2

45. Sokkalingam R, Muthupandi V, Sivaprasad K, Prashanth KG (2019) Dissimilar welding of Al0.1CoCrFeNi high-entropy alloy and AISI304 stainless steel. J Mater Res 34:2683–2694. https://doi.org/10.1557/jmr.2019.186

46. Ye Q, Feng K, Li Z et al (2017) Microstructure and corrosion properties of CrMnFeCoNi high entropy alloy coating. Appl Surf Sci 396:1420–1426. https://doi.org/10.1016/J.APSUSC.2016.11.176

47. Zhang S, Ma P, Jia Y et al (2019) Microstructure and mechanical properties of Al-(12–20)Si Bi-material fabricated by selective laser melting. Materials (Basel) 12:2126. https://doi.org/10.3390/ma12132126

48. Sokkalingam R, Mastanaiah P, Muthupandi V et al (2020) Electron-beam welding of high-entropy alloy and stainless steel: microstructure and mechanical properties. Mater Manuf Process 35:1885–1894. https://doi.org/10.1080/10426914.2020.1802045

49. Zhao C, Wang Z, Li D et al (2020) Cu-Ni-Sn alloy fabricated by melt spinning and selective laser melting: a comparative study on the microstructure and formation kinetics. J Mater Res Technol 9:13097–13105. https://doi.org/10.1016/j.jmrt.2020.09.047

50. Shamsujjoha M, Agnew SR, Fitz-Gerald JM et al (2018) High strength and ductility of additively manufactured 316L stainless steel explained. Metall Mater Trans A Phys Metall Mater Sci 49:3011–3027. https://doi.org/10.1007/s11661-018-4607-2

51. Suryawanshi J, Prashanth KG, Ramamurty U (2017) Mechanical behavior of selective laser melted 316L stainless steel. Mater Sci Eng A 696:113–121. https://doi.org/10.1016/j.msea.2017.04.058

52. Zhong Y, Rännar LE, Liu L et al (2017) Additive manufacturing of 316L stainless steel by electron beam melting for nuclear fusion applications. J Nucl Mater 486:234–245. https://doi.org/10.1016/J.JNUCMAT.2016.12.042

53. Yu S, Zhang P, Qiu K et al (2018) Preparation and characterization of 316L spherical powder for different uses by supersonic laminar flow atomization. Ferroelectrics 530:25–31. https://doi.org/10.1080/00150193.2018.1454071

54. Liu Y, Yang Y, Mai S et al (2015) Investigation into spatter behavior during selective laser melting of AISI 316L stainless steel powder. Mater Des 87:797–806. https://doi.org/10.1016/j.matdes.2015.08.086

55. Savage SJ, Froes FH (1984) Production of rapidly solidified metals and alloys. JOM J Miner Met Mater Soc 36:20–33. https://doi.org/10.1007/BF03338423

56. Yang X, Ge Y, Lehtonen J, Hannula SP (2020) Hierarchical microstructure of laser powder bed fusion produced face-centered-cubic-structured equiatomic crfenimn multicomponent alloy. Materials (Basel) 13:1–11. https://doi.org/10.3390/ma13204498

57. Kelly TF, Cohen M, Vander Sande JB (1984) Rapid solidification of a droplet-processed stainless steel. Metall Trans A Phys Metall Mater Sci 15A:819–833. https://doi.org/10.1007/BF02644556

58. Raghavan V (1995) Effect of manganese on the stability of austenite in Fe-Cr-Ni alloys. Metall Mater Trans A 26:237–242. https://doi.org/10.1007/BF02664662

59. Prashanth KG, Scudino S, Eckert J (2017) Defining the tensile properties of Al-12Si parts produced by selective laser melting. Acta Mater 126:25–35. https://doi.org/10.1016/j.actamat.2016.12.044

60. Sokkalingam R, Muthupandi V, Sivaprasad K, Prashanth KG (2019) Dissimilar welding of Al0.1CoCrFeNi high-entropy alloy and AISI304 stainless steel. J Mater Res 35:2683–2694. https://doi.org/10.1557/jmr.2019.186

61. Kocks UF, Mecking H (2003) Physics and phenomenology of strain hardening: the FCC case. Prog Mater Sci 48:171–273. https://doi.org/10.1016/S0079-6425(02)00003-8

62. Konda Gokuldoss P (2019) Work hardening in selective laser melted Al-12Si alloy. Mater Des Process Commun 1:e46. https://doi.org/10.1002/mdp2.46

63. Sokkalingam R, Mishra S, Cheethirala SR et al (2017) Enhanced relative slip distance in gas-tungsten-arc-welded Al0.5CoCrFeNi high-entropy alloy. Metall Mater Trans A 488:3630–3634. https://doi.org/10.1007/S11661-017-4140-8

64. Thapliyal S, Nene SS, Agrawal P et al (2020) Damage-tolerant, corrosion-resistant high entropy alloy with high strength and ductility by laser powder bed fusion additive manufacturing. Addit Manuf 36:101455. https://doi.org/10.1016/j.addma.2020.101455